PCCP

ROYAL SOCIETY OF CHEMISTRY

PAPER

View Article Online
View Journal | View Issue



Cite this: *Phys. Chem. Chem. Phys.*, 2024, **26**, 16521

# Quantum chemical modeling of enantioselective sulfoxidation and epoxidation reactions by indole monooxygenase *Vp*IndA1†

Qinrou Li, [ab] Shiqing Zhang, [bc] Fufeng Liu, [a] Hao Su [bc] and Xiang Sheng *[bc]

Indole monooxygenases (IMOs) are enzymes from the family of Group E monooxygenases, requiring flavin adenine dinucleotide (FAD) for their activities. IMOs play important roles in both sulfoxidation and epoxidation reactions. The broad substrate range and high selectivity of IMOs make them promising biocatalytic tools for synthesizing chiral compounds. In the present study, quantum chemical calculations using the cluster approach were performed to investigate the reaction mechanism and the enantioselectivity of the IMO from *Variovorax paradoxus* EPS (*Vp*IndA1). The sulfoxidation of methyl phenyl sulfide (MPS) and the epoxidation of indene were chosen as the representative reactions. The calculations confirmed that the $FAD_{OOH}$ intermediate is the catalytic species in the *Vp*IndA1 reactions. The oxidation of MPS adopts a one-step mechanism involving the direct oxygen-transfer from $FAD_{OOH}$ to the substrate and the proton transfer from the –OH group back to FAD, while the oxidation of indene follows a stepwise mechanism involving a carbocation intermediate. It was computationally predicted that *Vp*IndA1 prefers the formation of (*S*)-product for the MPS sulfoxidation and (1*S*,2*R*)-product for the indene epoxidation, consistent with the experimental observations. Importantly, the factors controlling the stereo-preference of the two reactions are identified. The findings in the present study provide valuable insights into the *Vp*IndA1-catalyzed reactions, which are essential for the rational design of this enzyme and other IMOs for industrial applications. It is also worth emphasizing that the quantum chemical cluster approach is again demonstrated to be powerful in studying the enantioselectivity of enzymatic reactions.

Received 6th February 2024,
Accepted 1st May 2024

DOI: 10.1039/d4cp00552j

rsc.li/pccp



## 1. Introduction

The synthesis of chiral compounds is one of the most attractive fields within the scientific community. The generally low efficiency and low yield in obtaining enantiomerically enriched chemicals pose challenges to asymmetric synthesis. Employing enzymatic reactions emerges as an effective and environmentally benign strategy to overcome the limitations of traditional asymmetric synthesis methods.[1–6] Indole monooxygenases (IMOs), a subclass of Group E monooxygenases, were identified in nature to catalyze the oxidation of indole and styrene in their degradation pathways.[7–9] These enzymes attract much attention owing to their capacities in catalyzing the enantioselective sulfoxidation and epoxidation reactions.[10] The broad substrate scope and high enantioselectivity of IMOs further increase their potential as biocatalytic tools for synthesizing chiral products.[11]

IMOs are members of the flavoprotein monooxygenase (FPMO) family, relying on the cofactor flavin adenine dinucleotide (FAD) for their catalytic abilities.[12] The typical catalytic cycle for FPMOs includes the activation of $O_2$ forming a flavin-OO(H) intermediate and incorporating an oxygen atom into the substrate.[10,13,14] In contrast to more studied members of the FPMO family, such as Baeyer–Villiger monooxygenases (BVMOs) and *p*-hydroxybenzoate hydroxylase (PHBH),[15–17] IMOs have received comparatively less attention. To promote the application of IMOs, it is crucial to conduct further investigations into the specific reactions catalyzed by these enzymes and to explore the factors responsible for the stereoselectivity in detail.

Recently, an IMO from the bacterium *Variovorax paradoxus* EPS (*Vp*IndA1) was identified[12] and the crystal structures of *Vp*IndA1 were subsequently reported in various forms.[18] Structure analysis showed that the binding pocket comprises a number of nonpolar residues such as Phe50, Phe191, Phe201,

[a] *College of Biotechnology, Tianjin University of Science and Technology, Tianjin, 300457, P. R. China*
[b] *Tianjin Institute of Industrial Biotechnology, Chinese Academy of Sciences, Tianjin 300308, P. R. China. E-mail: shengx@tib.cas.cn*
[c] *National Center of Technology Innovation for Synthetic Biology, National Engineering Research Center of Industrial Enzymes and Key Laboratory of Engineering Biology for Low-Carbon Manufacturing, Tianjin 300308, P. R. China*

† Electronic supplementary information (ESI) available. See DOI: https://doi.org/10.1039/d4cp00552j

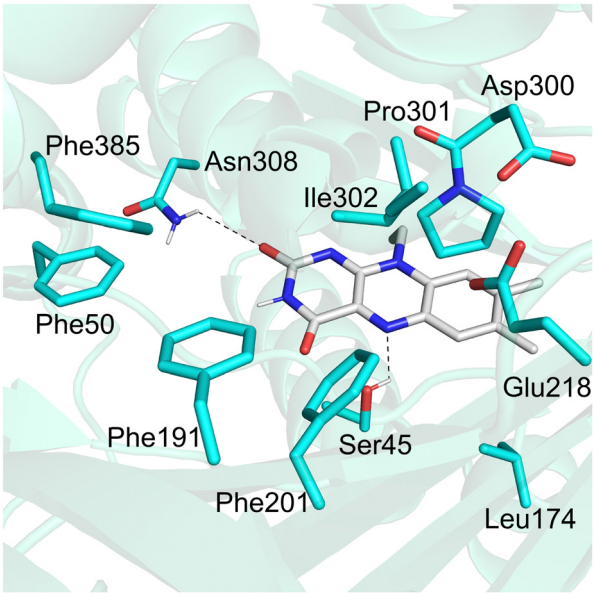


Fig. 1 Active site of the wide-type *Vp*IndA1 in complex with the FAD cofactor (PDB: 7Z4X).

Leu174, and Phe385.[18] Additionally, two ionizable residues (Glu218 and Asp300) that directly interact with each other are also found in the vicinity of the active site (Fig. 1).

The *Vp*IndA1 was demonstrated to be capable of converting methyl phenyl sulfide (MPS) to the (*S*)-enantiomer of methyl phenyl sulfoxide (MPSO) in the sulfoxidation reaction and converting indene to the (1*S*,2*R*)-enantiomer of indene oxide (IO) in the epoxidation reaction.[12,18] The reactions were proposed to follow the generally accepted catalytic cycle of FPMOs, wherein the dioxygen is activated to form a peroxide intermediate with flavin.[14] Based on the molecular mechanics (MM) force field calculations, the stereo-preferences of *Vp*IndA1 were rationalized by the geometric arrangements and the binding energies of different modes of the substrate.[18] Advantageous variants were then designed for improved substrate acceptance and stereoselectivity.[18]

Although the FPMO-catalyzed reactions have been extensively studied by using different experimental techniques,[10–23] there remains a debate regarding the protonation state of the peroxide in the intermediate after the activation of dioxygen by flavin. Namely, it is not clear that the catalytically relevant species is a flavin C4a-hydroperoxide ($FAD_{OOH}$) or a flavin C4a-peroxide ($FAD_{OO^-}$) intermediate. By using the double-mixing stopped-flow technique, it was demonstrated that both species are involved in the reaction of the cyclohexanone oxidation catalyzed by cyclohexanone monooxygenase (CHMO), but only the $FAD_{OO^-}$ is capable of oxygenating cyclohexanone.[19] In contrast, on the basis of the rapid acid quench in conjunction with the stopped-flow absorbance and fluorescence, it was suggested that the intermediate participating in the styrene epoxidation by styrene monooxygenase (SMO) is $FAD_{OOH}$.[20] The involvement of this intermediate in the catalysis was also proposed for the hydroxylation reactions catalyzed by other FPMOs.[21–23] For *Vp*IndA1, the focused FPMO in the present study, the catalytically relevant species in the reaction, remains an open question. Furthermore, *Vp*IndA1 exhibits high stereoselectivity toward various substrates.[11] However, the origins of the enantioselectivity of *Vp*IndA1 are obscure.

Various computational chemical methods, such as the hybrid quantum mechanics/molecular mechanics (QM/MM) method, the molecular dynamics (MD) simulation, and the quantum chemical cluster approach, have been used to model FPMO-catalyzed reactions.[24–27] Herein, the cluster approach is employed to investigate the enantioselective sulfoxidation and epoxidation reactions catalyzed by *Vp*IndA1. This method has been validated as a powerful tool in studying the enantioselectivity of widely distributed enzymes.[28–31] As the addition of $O_2$ to FAD has been established to be rapid both experimentally and computationally,[18,32,33] the current study specifically delves into the oxidation processes of MPS and indene after the activation of $O_2$ by FAD (Scheme 1). For the resulting peroxide intermediate, both protonated and deprotonated states are considered. Importantly, the enantioselectivities of *Vp*IndA1 toward MPS and indene are perfectly reproduced by the calculations, and the factors favoring the formation of the (*S*)-enantiomer of MPSO in the sulfoxidation reaction and the (1*S*,2*R*)-enantiomer of IO in the epoxidation reaction are rationalized by detailed analysis on the optimized structures of the transition states and intermediates.

## 2. Computational methods

### 2.1 Technical details

All the calculations in the current study were performed by using the Gaussian16 C.01 program[34] with the B3LYP-D3(BJ) density functional method.[35–38] Geometry optimizations were carried out with the 6-31G(d,p) basis set. At the same level as geometry optimization, the single-point energies using the SMD solvation model[39] with $\varepsilon = 4$ were calculated to estimate

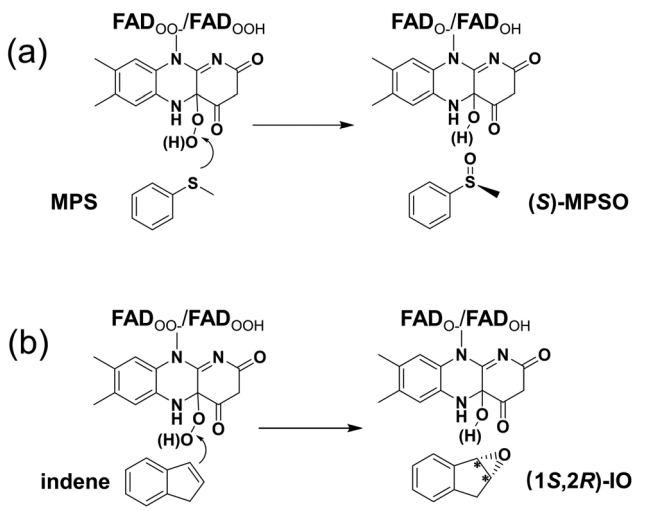


Scheme 1 The *Vp*IndA1-catalyzed reactions investigated in the present study: (a) the enantioselective sulfoxidation of methyl phenyl sulfide (MPS) and (b) the enantioselective epoxidation of indene.

 

the effect of surroundings. Frequency calculations were performed to obtain zero-point energies (ZPEs) and to characterize the nature of the intermediates and transition states (TSs), ensuring the presence of only positive frequencies for intermediates and only one imaginary frequency for TSs. The animations illustrating the vibrations corresponding to the imaginary frequency are provided in the Supplementary files. Intrinsic reaction coordinate (IRC) analysis was conducted to validate that the TSs connect the right local minima (Fig. S17 and S18, ESI†). Single-point calculations with the large basis set 6-311+G(2d,2p) were carried out to obtain more accurate electronic energies, which were then corrected for SMD solvation and ZPE corrections. The obtained final energies are reported in the present study. All the figures of the optimized structures were prepared by using Open-Source Pymol (**https://pymol.org/**).

### 2.2 Active site model

The active site model of the enzyme bound with the cofactor and substrate was designed based on the structure of wide-type *Vp*IndA1 crystallized with FAD (PDB ID: 7Z4X).[18] The substrate, MPS for the sulfoxidation reaction or indene for the epoxidation reaction, was manually incorporated into the respective model, and the FAD was modified to its $FAD_{OO^-}$ or $FAD_{OOH}$ form. The residues making up the binding sites of FAD and substrate are included in the active site model (Ser45, Ser46, Cys48, Phe50, Ile75, Leu172, Leu174, Val189, Phe191, Phe201, Phe203, Val216, Glu218, Asp300, Pro301, Ile302, Thr303, Gly304, Gln305, Asn308 and Phe385), as schematically drawn in Fig. 2.

According to the results from the constant pH molecular dynamics (CpHMD) simulations and the PROPKA sever, the Glu218 residue was modeled in the protonated state and the Asp300 residue was modeled in the ionized form (see the details in the ESI†). In the present study, different protonation states were considered for the peroxide intermediate after $O_2$ activation by FAD, which is the starting structure for the investigation of mechanism and enantioselectivity. Specifically, the two examined species are C(4a)-hydroperoxide ($FAD_{OOH}$) and C(4a)-peroxide ($FAD_{OO^-}$). The chirality of C(4a) was determined by analyzing the crystal structure (PDB ID: 7Z4X),[18] wherein the hydroperoxide/peroxide group is oriented toward the binding pocket of the substrate. For the model with $FAD_{OOH}$ and $FAD_{OO^-}$, the overall charge of the system is −1 and −2, respectively. The active site model comprises 351 atoms or 350 atoms for the system with MPS depending on the protonation state of the peroxide intermediate, and 345 atoms or 344 atoms for the system with indene.

The $FAD_{OO^-}$/$FAD_{OOH}$ and amino acids were truncated in the cluster model, and the hydrogen atoms saturating the truncated carbon were added manually. The truncated carbon and some associated hydrogen atoms were fixed during the geometry optimization processes to avoid unrealistic deviation from the crystal structure (see the fixed atoms in Fig. S1, ESI†). To ensure that the most favorable pathway is reported, geometries with different conformations of the substrate and active site residues were optimized for all the species along the reaction pathways and the lowest-energy one was reported for each species.

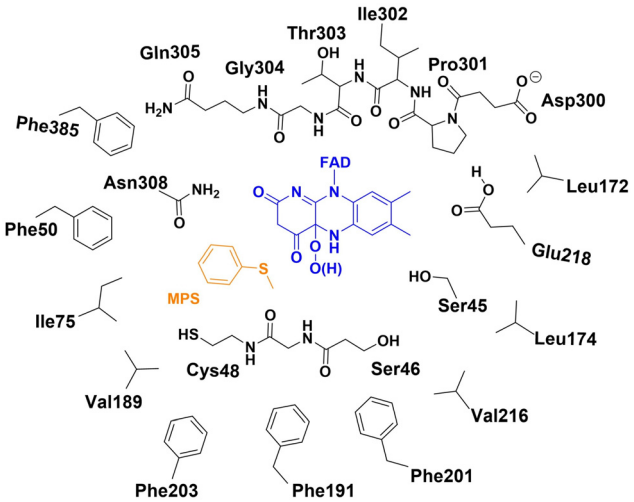


Fig. 2 The schematic representation of the active site model for the enzyme bound with $FAD_{OO^-}$/$FAD_{OOH}$ and MPS.

## 3. Results and discussion

As mentioned above, the protonation state of the peroxide in the intermediate after the activation of dioxygen by flavin remains uncertain. Considering this ambiguity, both the protonated ($FAD_{OOH}$) and deprotonated ($FAD_{OO^-}$) forms of the peroxide intermediate were considered in the investigation of the mechanism and enantioselectivity of *Vp*IndA1 toward MPS. Interestingly, calculations starting with $FAD_{OOH}$ perfectly reproduced the experimental results, specifically favoring the (*S*)-MPSO enantiomer of the product (Fig. 3 and 4). Conversely, the computationally predicted outcome based on $FAD_{OO^-}$, yielding (*R*)-MPSO, is inconsistent with the experimental observation (Fig. S2, ESI†). In the case of indene, the computational results starting from $FAD_{OOH}$ and $FAD_{OO^-}$ both reproduced the trend of the experimental stereoselective outcome; however, the pathway with $FAD_{OOH}$ exhibits a lower barrier compared to that with $FAD_{OO^-}$ (Fig. S3, ESI†). It can thus be concluded that it is more possible for the protonated $FAD_{OOH}$ to be the catalytically involved species in the catalysis. In the following section, the calculation results of the reactions stemming from $FAD_{OOH}$ are discussed in detail and the results starting with $FAD_{OO^-}$ are briefly presented.

### 3.1 Binding mode of MPS in the active site of *Vp*InA1

To achieve the lowest-energy binding mode, a large number of structures with different conformations of the active site residues and substrates in the active site were optimized and their energies were compared (Fig. 3 for the lowest-energy structures and Fig. S4 for the others, ESI†). The obtained structures can be classified into two types depending on the direction of the MPS phenyl group pointing toward, named "Phenyl-left" mode and "Phenyl-right" mode. The phenyl ring faces toward Phe50 in the "Phenyl-left" mode (Fig. 3a) and toward Phe201 in the "Phenyl-right" mode (Fig. 3b). Depending on how the methyl group of MPS faces the peroxide in the $FAD_{OOH}$ intermediate, either *S*- or *R*-products will be preferred. For each mode, it was found that the methyl group of MPS can be located at different positions, which decides

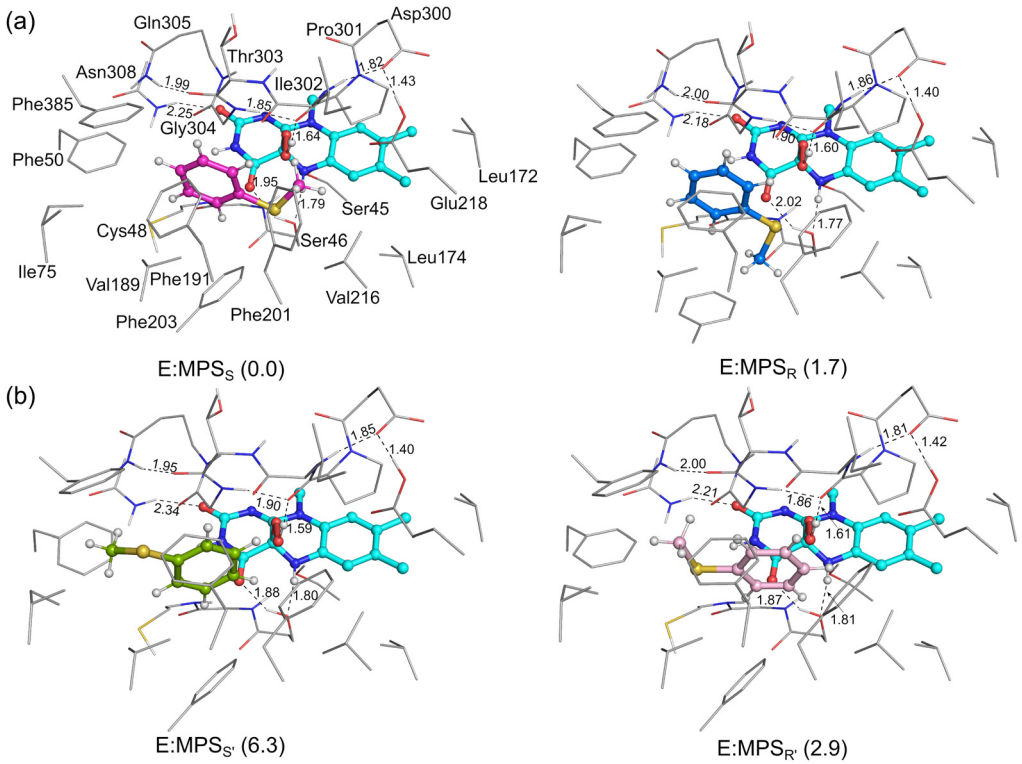


Fig. 3 Optimized structures of the lowest-energy **E:MPS** complexes with the "Phenyl-left" mode (a) and with the "Phenyl-right" mode (b). The subscript S (in **E:MPS$_S$** and **E:MPS$_{S'}$**) and the subscript R (in **E:MPS$_R$** and **E:MPS$_{R'}$**) denote the configurations of the respective products originating from this ES complex. The energies, which are provided in parentheses in kcal mol$^{-1}$, are relative to **E:MPS$_S$**. For clarity, most of the hydrogen atoms are omitted in the figure. Selected distances are given in Å.

whether the *re* or the *si* face to be attacked by the peroxide in the following oxidation process. For example, in the "Phenyl-left" mode, the binding of the methyl group in the vicinity of Ile302 leads to the peroxide group being located at the *si* face of the sulfur, and the binding in the vicinity of Phe203 results in the peroxide group being at the *re* face, for which the oxygen-transfer from the peroxide gives *S*- and *R*-products, respectively.

A number of enzyme-substrate complexes with relatively low energies were considered for the studies of the sulfoxidation mechanism and enantioselectivity. It was shown that the pathways starting from all the considered structures with "Phenyl-right" mode are associated with prohibitively high barriers and this mode is thus not productive (Fig. S5, ESI†). In contrast, the pathways with the "Phenyl-left" mode were calculated to have reasonable barriers. The lowest-energy structures for the complexes leading to the formation of *R*- and *S*-products (called **E:MPS$_R$** and **E:MPS$_S$**, respectively) are shown in Fig. 3a. These two structures show high similarities in the hydrogen bond networks between FAD and the active site residues (Ser46 and Asn308). However, in **E:MPS$_S$**, the methyl group of MPS is located close to Ile302, while in **E:MPS$_R$**, it orients toward Phe203, leading to an unfavorable steric hindrance. This results in a higher energy of **E:MPS$_R$** than **E:MPS$_S$** by 1.7 kcal mol$^{-1}$.

### 3.2 Mechanism and enantioselectivity of *Vp*InA1 toward MPS

As mentioned above, a number of starting structures were considered for the following study on the oxidation mechanism and selectivity. The calculations showed that the *Vp*InA1-catalyzed sulfoxidation is a concerted process that involves the attack of the –OH group of the FAD$_{OOH}$ at the sulfur of MPS, leading to the S–O bond formation and the O–O bond cleavage. Simultaneously, the proton of –OH transfers back to FAD, giving FAD$_{OH}$ in the enzyme-product complexes. This concerted mechanism is consistent with the previous proposal on the other enzymes from the same family.[24,25,40] We also attempted to obtain an intermediate without involving the proton transfer, in which case the reaction would follow a stepwise mechanism. However, upon optimization, the proton spontaneously transfers from the –OH group back to FAD. The calculated energies of the lowest-energy transition states (TSs) corresponding to the formation of (*S*)-MPSO (**MPS-TS$_S$**) and (*R*)-MPSO (**MPS-TS$_R$**) are 7.3 kcal mol$^{-1}$ and 16.3 kcal mol$^{-1}$, respectively, relative to **E:MPS$_S$** (Fig. 4a). Namely, the formation of the (*S*)-product is much more favored by the reaction compared to the (*R*)-enantiomer. This trend is indeed consistent with the experimentally observed stereopreference for *S*-enantiomer with a measured ee value of higher than 99%. Other optimized TS structures with higher energies are provided in Fig. S6, ESI.† The resulting enzyme-product complexes (**E:MPSO$_S$** and **E:MPSO$_R$**) have energies of −43.4 kcal mol$^{-1}$ and −33.3 kcal mol$^{-1}$ relative to **E:MPS$_S$** for the *S*- and *R*-enantiomers, respectively (Fig. S7, ESI†).

By scrutinizing the optimized structures of **MPS-TS$_S$** and **MPS-TS$_R$**, the key factors influencing the enantioselectivity of *Vp*InA1 are unveiled. First, it should be emphasized that the

 

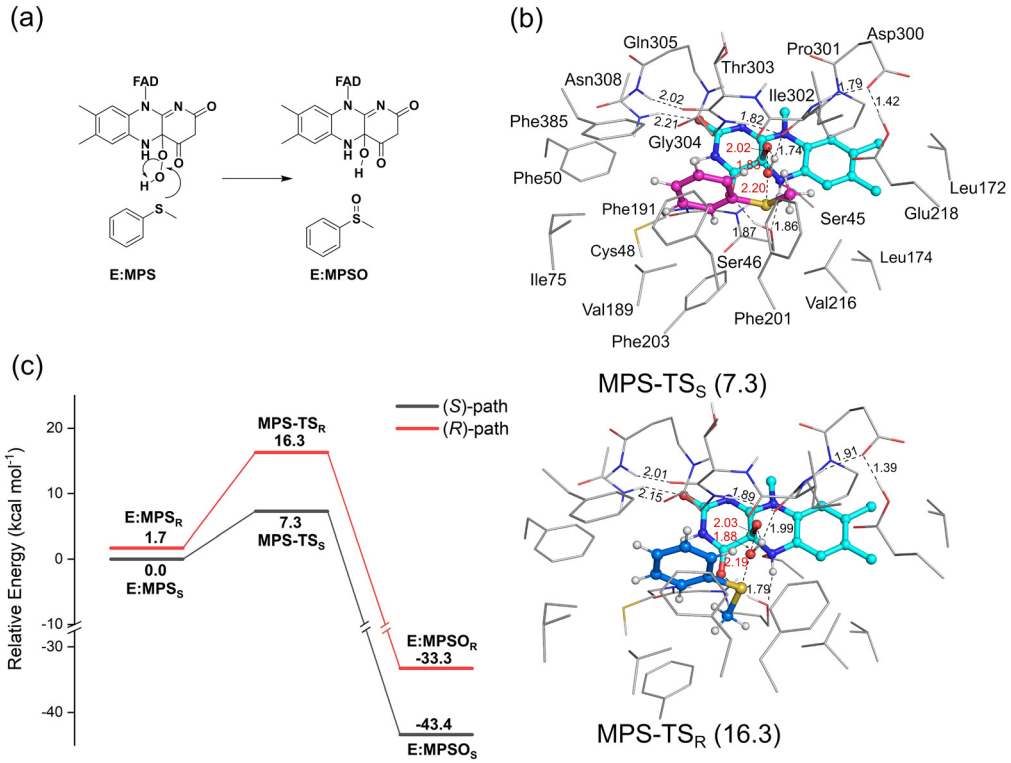


Fig. 4 (a) Mechanism of the *Vp*InA1-catalyzed sulfoxidation of MPS and (b) the optimized structures of **MPS-TS$_S$** and **MPS-TS$_R$**. (c) The calculated energy profiles for the *Vp*InA1-catalyzed sulfoxidation of MPS, in which the pathways leading to the formation of (*S*)- and (*R*)-MPSO are shown in black and red, respectively. The energies relative to **E:MPS$_S$** are provided in parentheses in kcal mol$^{-1}$. For clarity, most of the hydrogen atoms are omitted in the figure. Selected distances are given in Å.

phenyl group of the substrate is restricted in the binding pocket by the π–π interactions with surrounding aromatic residues (Phe50, Phe191, Phe201 and Phe385) and consequently occupies similar positions in **MPS-TS$_R$** and **MPS-TS$_S$**. However, the methyl group exhibits distinct orientations and can thus develop different interactions with nearby groups in two transition states. In **MPS-TS$_R$**, unfavorable steric hindrances are identified between the methyl group of the substrate and the flavin group of the cofactor, as well as the Phe203 residue (Fig. 4b for the optimized structures and Fig. S8 (ESI†) for the schematic representation). Furthermore, the transferring –OH group experiences greater stabilization in **MPS-TS$_S$** than in **MPS-TS$_R$**, as evidenced by the shorter distance of the hydrogen bond with the backbone carbonyl group of Pro301 in the former (1.74 Å) than the latter (1.99 Å). It is interesting to note that in *Pp*StyA, a styrene monooxygenase (SMO) from *Pseudomonas putida* that exhibits *R*-enantiopreference toward MPS, the substrate binding pocket is mainly composed of less bulky residues (see a structural comparison in Fig. S9, ESI†),[41,42] allowing the substrate to dynamically adjust its conformation during the reaction. Specifically, the equivalent position of Phe203 in *Vp*InA1 is found to be occupied by a small amino acid isoleucine. These differences provide additional support for the rationale behind the enantioselectivity of *Vp*InA1 toward MPS.

### 3.3 Mechanism and enantioselectivity of *Vp*InA1 toward indene

Following the strategy in the study of the sulfoxidation reaction, a number of structures with different orientations of indene were considered in the calculations to ensure that the lowest-energy binding mode was obtained. Similar to that for MPS, the binding modes of indene to *Vp*InA1 can also be classified into two types: "Phenyl-left" mode and "Phenyl-right" mode, in which the phenyl ring of indene faces toward Phe50 and Phe201, respectively (Fig. S10 and S11 for optimized structures, ESI†). Depending on how the methylene group of indene orientates, the binding modes can lead to the formation of either (1*S*,2*R*)- or (1*R*,2*S*)-IO. Taking the "Phenyl-left" mode as an illustration, when the methylene group of indene is directed toward Phe203, it leads to the formation of (1*S*,2*R*)-IO, whereas an orientation toward Ile302 yields (1*R*,2*S*)-IO.

Similar to the sulfoxidation reaction catalyzed by *Vp*InA1, the lowest-energy **E:indene$_{1R,2S}$** complex, which results in the formation of (1*R*,2*S*)-IO, falls into the "Phenyl-left" type (Fig. S10, ESI†). The calculated energy of **E:indene$_{1S,2R}$** leading to the other enantiomer (1*S*,2*R*)-IO is 0.9 kcal mol$^{-1}$ higher than that of **E:indene$_{1R,2S}$**. Structure analysis showed that the two complexes have comparable hydrogen bond networks within the active site. However, the difference in the orientation of the methylene group of indene in the two structures leads to an undesirable steric hindrance between the methylene group and nearby residues in **E:indene$_{1S,2R}$**, which is not present in **E:indene$_{1R,2S}$**. Again, similar to the sulfoxidation reaction, the pathways of indene epoxidation with the "Phenyl-right" mode are associated with prohibitively high barriers (Fig. S12, ESI†) and this mode is not productive here either.

The calculations reveal that the indene epoxidation catalyzed by *Vp*InA1 follows a stepwise mechanism involving a

carbocation intermediate. Specifically, the reaction pathway initiates with the –OH group of $FAD_{OOH}$ attacking the C=C bond of indene, forming a carbocation intermediate, succeeded by a proton transfer from the –OH group back to FAD. According to the calculations, the proton transfer is a barrier-less process and the final product has an energy of *ca.* 20 kcal $mol^{-1}$ lower than that of the intermediate, indicating that the carbocation intermediate will rapidly convert to the final product once formed. The lowest-energy TSs resulting in the formation of (1*R*,2*S*)-product (**indene-TS$_{1R,2S}$**) and (1*S*,2*R*)-product (**indene-TS$_{1S,2R}$**) have energies of 16.6 kcal $mol^{-1}$ and 13.4 kcal $mol^{-1}$, respectively, relative to **E:indene$_{1R,2S}$** (Fig. 5, see other optimized TS structures in Fig. S13, ESI†). Namely, the pathway leading to the (1*S*,2*R*)-product is 3.2 kcal $mol^{-1}$ lower than that of the (1*R*,2*S*)-product. Experimentally, the (1*S*,2*R*)-enantiomer was indeed the preferred product with an ee value of 35%. The computational trend is thus in agreement with the experimental results.

Experimentally, the Phe191Met/Phe201Leu/Ile302Val mutant exhibited an increased stereo-selectivity with an ee value of 99.80%.[18] Using the same active site model and methodology mentioned above, the reaction pathways of this mutant were also studied (Fig. S16 for the optimized structures, ESI†). The calculated energy difference between the two TSs increases from 3.2 kcal $mol^{-1}$ for the wide-type enzyme to 7.2 kcal $mol^{-1}$ for the mutant, reproducing thus the experimental trend. These results emphasize the robust capabilities of the quantum chemical cluster approach in elucidating the enantioselectivity of enzymatic reactions.

It is worth noting that the trends observed in the energies of **E:indene** and **E:IO** in the pathways leading to two enantiomers are reversed compared to the TSs that dictate the enantiopreference of the reaction. Therefore, relying solely on the energies of **E:indene** and **E:IO** for rationalizing the enantioselectivity of *Vp*InA1 is misleading. This highlights the importance of investigating the entire reaction pathway to accurately pinpoint the factors controlling selectivity. Similar conclusions have also been drawn from the quantum chemical studies on other enzymes.[43,44]

## 4. Conclusions

The broad substrate range and high selectivity of indole monooxygenases (IMOs) make them valuable candidates for asymmetric synthesis. Nevertheless, the unclear reaction mechanisms, along with the ambiguous origin of the enantioselectivity, have hindered their industrial applications. In the present work, the sulfoxidation and indene epoxidation catalyzed by the IMO from *Variovorax paradoxus* EPS (*Vp*IndA1), an enzyme from the family of IMOs, are studied by using the quantum chemical cluster approach.

The calculations show that the protonated $FAD_{OOH}$ rather than the deprotonated $FAD_{OO^-}$ is the catalytically relevant species in the *Vp*IndA1-catalyzed reactions. For both methyl phenyl sulfide (MPS) and indene substrates, the preferred binding mode is that the phenyl ring on the substrate is orientated toward Phe50. Mechanistic investigations reveal

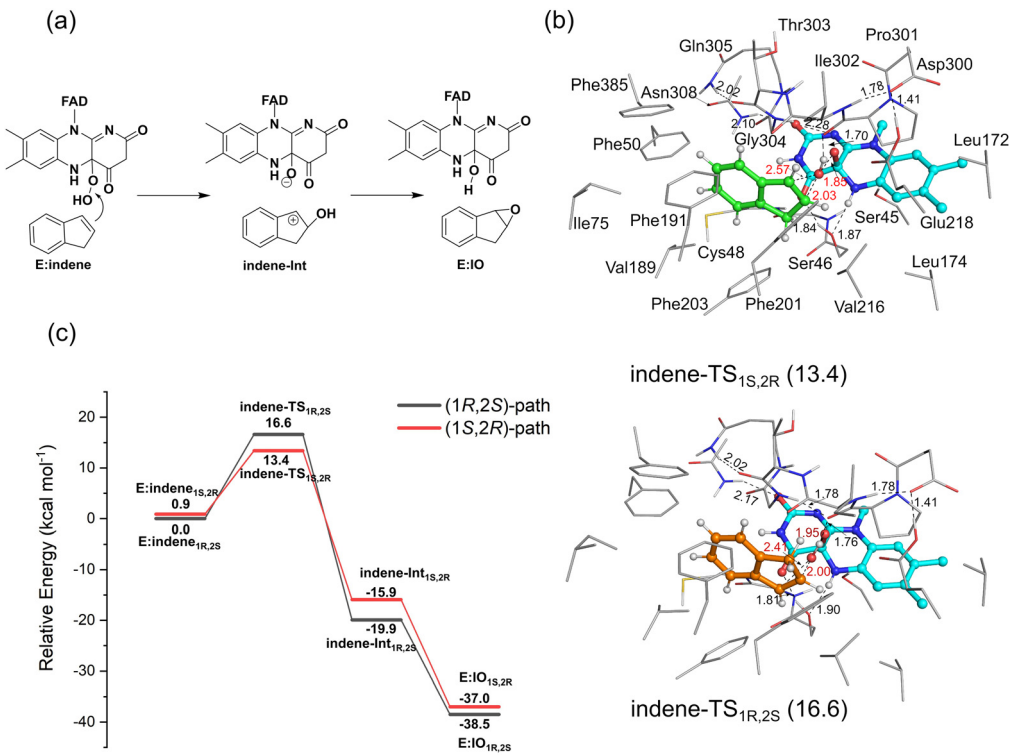


Fig. 5 (a) Mechanism of the *Vp*InA1-catalyzed indene epoxidation and (b) the optimized structures of **indene-TS$_{1R,2S}$** and **indene-TS$_{1S,2R}$**. The energies, provided in parentheses in kcal $mol^{-1}$, are all referenced relative to **E:indene$_{1R,2S}$**. (c) The calculated energy profiles for the *Vp*InA1-catalyzed indene epoxidation, in which the pathways leading to the formation of (1*R*,2*S*)- and (1*S*,2*R*)-IO are shown in black and red, respectively. For clarity, most of the hydrogen atoms are omitted in the figure. Selected distances are given in Å.

 

distinct pathways for the substrate oxidation by *Vp*InA1. The oxidation of MPS follows a one-step mechanism, consisting of the direct oxygen transfer from $FAD_{OOH}$ to the substrate, accompanied by proton transfer of the –OH group back to FAD. In contrast, the oxidation of indene proceeds via a stepwise mechanism involving a carbocation intermediate. Upon analyzing the optimized structures of the corresponding transition states, it can be concluded that the aromatic residues within the active site, especially Phe203, play significant roles in controlling the enantioselectivity of *Vp*IndA1.

The details of the reaction mechanisms obtained in the present study provide valuable information on the IMO-catalyzed reactions. It holds considerable significance in facilitating the systematic design of enzyme variants with tailored properties. The current study also emphasizes the robust capabilities of the quantum chemical cluster approach in elucidating the reaction mechanism and selectivity of enzymes.

## Author contributions

X. S. designed the project and supervised the project; Q. L. performed research and analyzed data; S. Z, F. L., and H. S. contributed also to the calculations and data analysis; Q. L. and X. S. wrote the paper.

## Conflicts of interest

There are no conflicts to declare.

## Acknowledgements

We gratefully acknowledge the National Key R&D Program of China (2021YFA0911500), the Tianjin Synthetic Biotechnology Innovation Capacity Improvement Project (TSBICIP-CXRC-026) and the National Natural Science Foundation of China (22103095) for the financial support. A portion of the calculations in this study were performed on the ORISE Supercomputer.

## References

1 C. M. Clouthier and J. N. Pelletier, *Chem. Soc. Rev.*, 2012, **41**, 1585–1605.
2 C. K. Winkler, J. H. Schrittwieser and W. Kroutil, *ACS Cent. Sci.*, 2021, **7**, 55–71.
3 M. Hall, *RSC Chem. Biol.*, 2021, **2**, 958–989.
4 S. Wu, R. Snajdrova, J. C. Moore, K. Baldenius and U. T. Bornscheuer, *Angew. Chem., Int. Ed.*, 2021, **60**, 88–119.
5 D. Yi, T. Bayer, C. P. S. Badenhorst, S. Wu, M. Doerr, M. Höhne and U. T. Bornscheuer, *Chem. Soc. Rev.*, 2021, **50**, 8003–8049.
6 A. R. Alcántara, P. Domínguez de María, J. A. Littlechild, M. Schürmann, R. A. Sheldon and R. Wohlgemuth, *ChemSusChem*, 2022, **15**, e202102709.
7 K. E. O'Connor, A. D. Dobson and S. Hartmans, *Appl. Environ. Microbiol.*, 1997, **63**, 4287–4291.
8 G.-H. Lin, H.-P. Chen and H.-Y. Shu, *PLoS One*, 2015, **10**, e0138798.
9 M. Sadauskas, J. Vaitekūnas, R. Gasparavičiūtė and R. Meškys, *Appl. Environ. Microbiol.*, 2017, **83**, e01453–e01417.
10 C. E. Paul, D. Eggerichs, A. H. Westphal, D. Tischler and W. J. H. van Berkel, *Biotechnol. Adv.*, 2021, **51**, 107712.
11 T. Heine, A. Scholtissek, S. Hofmann, R. Koch and D. Tischler, *ChemCatChem*, 2020, **12**, 199–209.
12 D. Tischler, R. Schwabe, L. Siegel, K. Joffroy, S. R. Kaschabek, A. Scholtissek and T. Heine, *Molecules*, 2018, **23**, 809.
13 A. Mattevi, *Trends Biochem. Sci.*, 2006, **31**, 276–283.
14 E. Romero, J. R. Gómez Castellanos, G. Gadda, M. W. Fraaije and A. Mattevi, *Chem. Rev.*, 2018, **118**, 1742–1769.
15 H. Leisch, K. Morley and P. C. K. Lau, *Chem. Rev.*, 2011, **111**, 4165–4222.
16 S. Montersino, D. Tischler, G. T. Gassner and W. J. H. van Berkel, *Adv. Synth. Catal.*, 2011, **353**, 2301–2319.
17 M. J. L. J. Fürst, A. Gran-Scheuch, F. S. Aalbers and M. W. Fraaije, *ACS Catal.*, 2019, **9**, 11207–11241.
18 J. Kratky, D. Eggerichs, T. Heine, S. Hofmann, P. Sowa, R. H. Weiße, D. Tischler and N. Sträter, *Angew. Chem., Int. Ed.*, 2023, **62**, e202300657.
19 D. Sheng, D. P. Ballou and V. Massey, *Biochemistry*, 2001, **40**, 11156–11167.
20 A. Kantz and G. T. Gassner, *Biochemistry*, 2011, **50**, 523–532.
21 M. G. Taylor and V. Massey, *J. Biol. Chem.*, 1990, **265**, 13687–13694.
22 J. Sucharitakul, P. Chaiyen, B. Entsch and D. P. Ballou, *J. Biol. Chem.*, 2006, **281**, 17044–17053.
23 R. Baron, C. Riley, P. Chenprakhon, K. Thotsaporn, R. T. Winter, A. Alfieri, F. Forneris, W. J. H. van Berkel, P. Chaiyen, M. W. Fraaije, A. Mattevi and J. A. McCammon, *Proc. Natl. Acad. Sci.*, 2009, **106**, 10603–10608.
24 A. C. C. Barbosa, R. P. P. Neves, S. F. Sousa, M. J. Ramos and P. A. Fernandes, *ACS Catal.*, 2018, **8**, 9298–9311.
25 Y. Özkılıç and N. Ş. Tüzün, *J. Phys. Chem. A*, 2019, **123**, 3149–3159.
26 A. Rodríguez Benítez, S. E. Tweedy, S. A. Baker Dockrey, A. L. Lukowski, T. Wymore, D. Khare, C. L. Brooks, III, B. A. Palfey, J. L. Smith and A. R. H. Narayan, *ACS Catal.*, 2019, **9**, 3633–3640.
27 Y. Dong, T. Li, S. Zhang, J. Sanchis, H. Yin, J. Ren, X. Sheng, G. Li and M. T. Reetz, *ACS Catal.*, 2022, **12**, 3669–3680.
28 F. Himo, *J. Am. Chem. Soc.*, 2017, **139**, 6780–6786.
29 X. Sheng and F. Himo, *J. Am. Chem. Soc.*, 2019, **141**, 11230–11238.
30 X. Sheng, M. Kazemi, F. Planas and F. Himo, *ACS Catal.*, 2020, **10**, 6430–6449.
31 X. Sheng and F. Himo, *Acc. Chem. Res.*, 2023, **56**, 938–947.
32 J. Sucharitakul, C. Tongsook, D. Pakotiprapha, W. J. H. van Berkel and P. Chaiyen, *J. Biol. Chem.*, 2013, **288**, 35210–35221.
33 S. Visitsatthawong, P. Chenprakhon, P. Chaiyen and P. Surawatanawong, *J. Am. Chem. Soc.*, 2015, **137**, 9363–9374.
34 M. J. Frisch, G. W. Trucks, H. B. Schlegel, G. E. Scuseria, M. A. Robb, J. R. Cheeseman, G. Scalmani, V. Barone,

G. A. Petersson, H. Nakatsuji, X. Li, M. Caricato, A. V. Marenich, J. Bloino, B. G. Janesko, R. Gomperts, B. Mennucci, H. P. Hratchian, J. V. Ortiz, A. F. Izmaylov, J. L. Sonnenberg, D. Williams-Young, F. Ding, F. Lipparini, F. Egidi, J. Goings, B. Peng, A. Petrone, T. Henderson, D. Ranasinghe, V. G. Zakrzewski, J. Gao, N. Rega, G. Zheng, W. Liang, M. Hada, M. Ehara, K. Toyota, R. Fukuda, J. Hasegawa, M. Ishida, T. Nakajima, Y. Honda, O. Kitao, H. Nakai, T. Vreven, K. Throssell, J. A. Montgomery Jr, J. E. Peralta, F. Ogliaro, M. J. Bearpark, J. J. Heyd, E. N. Brothers, K. N. Kudin, V. N. Staroverov, T. A. Keith, R. Kobayashi, J. Normand, K. Raghavachari, A. P. Rendell, J. C. Burant, S. S. Iyengar, J. Tomasi, M. Cossi, J. M. Millam, M. Klene, C. Adamo, R. Cammi, J. W. Ochterski, R. L. Martin, K. Morokuma, O. Farkas, J. B. Foresman and D. J. Fox, *Gaussian 16, Revision C.01*, Gaussian, Inc., Wallingford CT, 2016.

35 C. Lee, W. Yang and R. G. Parr, *Phys. Rev. B: Condens. Matter Mater. Phys.*, 1988, **37**, 785–789.

36 A. D. Becke, *J. Chem. Phys.*, 1993, **98**, 5648–5652.

37 S. Grimme, J. Antony, S. Ehrlich and H. Krieg, *J. Chem. Phys.*, 2010, **132**, 154104.

38 S. Grimme, S. Ehrlich and L. Goerigk, *J. Comput. Chem.*, 2011, **32**, 1456–1465.

39 A. V. Marenich, C. J. Cramer and D. G. Truhlar, *J. Phys. Chem. B*, 2009, **113**, 6378–6396.

40 R. D. Bach and O. Dmitrenko, *J. Phys. Chem. B*, 2003, **107**, 12851–12861.

41 U. E. Ukaegbu, A. Kantz, M. Beaton, G. T. Gassner and A. C. Rosenzweig, *Biochemistry*, 2010, **49**, 1678–1688.

42 J. Nikodinovic-Runic, L. Coulombel, D. Francuski, N. D. Sharma, D. R. Boyd, R. M. O. Ferrall and K. E. O'Connor, *Appl. Microbiol. Biotechnol.*, 2013, **97**, 4849–4858.

43 S. Moa and F. Himo, *J. Inorg. Biochem.*, 2017, **175**, 259–266.

44 M. Prejanò, X. Sheng and F. Himo, *ChemistryOpen*, 2022, **11**, e202100250.

 